# Combining shallow-water and analytical wake models for tidal array micro-siting

Connor Jordan, Davor Dundovic, Anastasia K. Fragkou, Georgios Deskos, Daniel S. Coles,
Matthew D. Piggott, Athanasios Angeloudis

# Combining shallow-water and analytical wake models for tidal array micro-siting

Connor Jordan[a], Davor Dundovic[b], Anastasia K. Fragkou[a], Georgios Deskos[c], Daniel S. Coles[d], Matthew D. Piggott[b], Athanasios Angeloudis[a,*]

[a] *School of Engineering, Institute for Infrastructure and the Environment, University of Edinburgh, Edinburgh, UK*
[b] *Department of Earth Science & Engineering, Imperial College London, London, UK*
[c] *National Wind Technology Center, National Renewable Energy Laboratory, Golden, Colorado, USA*
[d] *School of Engineering, Computing and Mathematics, University of Plymouth, Plymouth PL4 8AA, UK*

---

## Abstract

Array optimisation is critical for improving power performance and reducing infrastructure costs thereby helping enable tidal-stream energy to become a competitive renewable energy source. However, ascertaining an optimal array layout is a highly complex problem, subject to the specific site hydrodynamics characterisation and multiple inter-disciplinary constrains. In this work, we present a novel optimisation approach that combines an analytical-based wake model, *FLORIS*, with an ocean model, *Thetis*. The approach is demonstrated with applications of increasing complexity. By utilising the method of analytical wake superposition, the addition or alteration of turbine position does not require re-calculation of the entire flow field, thus allowing the use of simple heuristic techniques to perform optimisation at a fraction of the computational cost of more sophisticated methods. Using a custom condition-based placement algorithm, this methodology is applied to the Pentland Firth for 24 turbines with a rated speed of $3.05\,\mathrm{m\,s^{-1}}$, demonstrating practical implications whilst also considering the temporal variability of the tide. Micro-siting using this technique generated an array 12% more productive on average than a staggered layout, despite flow speeds regularly exceeding the rated value. Performance was further evaluated through assessment of the optimised layout within the ocean model that represents the turbines through a discrete turbine representation. Used iteratively, this methodology could be applied to deliver improved array configurations in a manner that accounts for local hydrodynamic effects.

*Keywords:* Array optimisation, Tidal turbines, *FLORIS*, Shallow water equations

---

## 1. Introduction

The levelised cost of energy (LCOE), defined as the average net present cost of electricity generation for a power plant over its lifetime, is often cited as a key metric for the competitiveness of an energy technology. Unless there is a rapid increase in installations, the LCOE for tidal-stream is set to remain at more than £150/MWh by 2025 (Smart and Noonan, 2018; Topper et al., 2021), whilst the LCOE for solar and both onshore and offshore wind will fall to approximately £25–£32/MWh (U.S. Energy Information Administation, 2020). Reducing LCOE is paramount if tidal-stream energy is to become a competitive, sustainable energy source. This could be achieved through several measures (Coles and Walsh, 2019; Goss et al.,

---

[*] Corresponding author
*Email address:* `a.angeloudis@ed.ac.uk` (Athanasios Angeloudis)

2020, 2021a,b): (i) physical infrastructure improvements, which could involve optimisation of the turbine design and operation, (ii) economies of scale in turbine design, (iii) economies of volume in manufacturing, operation and maintenance, (iv) technology innovation, (v) learning, and (vi) financing mechanisms. Turbines have now reached technology readiness levels of 7–8 (Chozas, 2015; SIMEC Atlantis Energy, 2020) and need to be tested in large arrays for extended periods of time in order to reach full maturity and facilitate implementation of the aforementioned cost reduction mechanisms. In supporting this, strategies should be investigated and developed for the reliable assessment of the the tidal resource (Neill et al., 2014; Robins et al., 2015) to reduce investment uncertainty, as well as array design optimisation to maximise performance. Array optimisation has already shown potential to increase array power by up to 33% relative to a regular aligned layout, albeit with power capping removed (Funke et al., 2014). Hence developing more robust, yet practical optimisation methods could be a key step to achieving further LCOE reductions.

Array power can be associated with up to eight controlling array effects, as outlined in Vennell et al. (2015). These include the reduction of free-stream velocity by the introduction of turbines and the relative size of the array in the channel. This leads to conflicting design performance interactions among turbines, particularly for large arrays that dominate channel dynamics. For example, minimising environmental impacts such as sediment transport may restrict array placement (Fairley et al., 2015; du Feu et al., 2019). Likewise, maintaining navigation routes through clearance constraints prevents exploitation of channel blockage, a hugely beneficial phenomenon for larger arrays. As such, array optimisation is often posed as a multi-objective problem, adding additional constraints to an already complex problem (Nash et al., 2014; Culley et al., 2016; du Feu et al., 2017, 2019; González-Gorbeña et al., 2018; Phoenix and Nash, 2019).

Ascertaining the optimal array layout becomes computationally intensive when interlinked with the hydrodynamics at the installation area as it presents a partial differential equation (PDE) constrained optimisation problem. Early work therefore involved simplified hydrodynamic models, as ‘in-concert’ tuning of tidal turbines in an array would necessitate multiple runs which would require appreciable time in more detailed models (Vennell, 2011, 2012). Investigations of channel-scale optimisation, such as a systematic exploration of optimal array layouts by conducting large numbers of 2-D simulations for different layouts and turbine tunings have been carried out using such models, but are hugely time and memory intensive (Divett et al., 2016). An alternative has been proposed by using gradient-based optimisation that makes use of adjoint methods to efficiently calculate the objective function gradient, leading to immense reductions in the number of evaluations required (Funke et al., 2014, 2016). This enables optimisation with a capacity to account for impacts to the hydrodynamics, at a much lower computational cost than techniques that estimate the gradient. The same approach has been adopted for wind farms to capture non-linear turbulent flow physics, as the adjoint method allows inclusion of higher fidelity 3D computational fluid dynamics (CFD) (King et al., 2017). Nevertheless, adjoint optimisation is still fairly intensive as demonstrated by examples in the literature, which are largely constrained to idealised and semi-idealised cases (Funke et al., 2014; Barnett et al., 2014).

To circumvent intense computational effort, inspiration can be taken from wind energy research, where surrogate models are used to simplify the governing physics. These models may ignore important hydrodynamic effects such as blockage that can augment power production for tidal energy (Nishino and Willden, 2012; Chen et al., 2019). For example, a duct effect may be exploited by placing turbines in a staggered arrangement, funnelling and accelerating the flow onto downstream turbines, as shown in Funke et al. (2014). Aside from certain examples restricted in idealised domains Stansby and Stallard (2016), semi-analytical methods based on turbine wake superposition principles are often constrained to a structured turbine placement (Lo Brutto et al., 2016). Nevertheless, the use of wake superposition methods has been found to give reasonable agreement to laboratory measurements for model tidal turbines. Rapid optimisation in idealised low-blockage cases has provided significant increases in array efficiency (Stansby and Stallard, 2016). González-Gorbeña et al. (2016) took a similar approach, applying a surrogate-based optimisation method in combination with a hydrodynamic model, but turbine placement has been limited to spacing parameters applied uniformly across the array to prevent significant increases in optimisation time.

In setting out this study, we outline our overarching goal: an array optimisation strategy that is computationally efficient and extensible to the multi-objective optimisation settings sought thereafter. Additionally, it must be reliable, accurate and not ignore important hydrodynamic factors that effect the optimal array design. This paper aims to demonstrate a novel optimisation approach, retrofitting an analytical wake model designed for wind array optimisation (*FLORIS* from the US National Renewable Energy Laboratory) for use in conjunction with a coastal ocean model (*Thetis*). We provide details on an optimisation approach which includes the option of a custom greedy algorithm for micro-siting purposes. This is applied to a suite of representative idealised cases, progressing to a practical study of the Inner Sound of the Pentland Firth, UK.

## 2. Methodology

We combine a depth-averaged hydrodynamic model, *Thetis*, with an analytical wake model, *FLORIS* (FLOw Redirection and Induction in Steady-state[1]). *FLORIS* is used to perform array optimisation by importing ambient flow fields from *Thetis*, whereas *Thetis* validates initial and optimised layouts, by simulating with the presence of turbines parameterised through additional turbine drag terms, and evaluating impacts on the flow field and array power. Both models rely on actuator disc theory to represent the tidal turbine rotor, however, differences between the two models exist, which necessitates the introduction of an intermediate calibration step. A schematic of the described coupled approach is shown in Figure 1.

### 2.1. Shallow Water Equation Modelling with Thetis

*Thetis*[2], is a 2D/3D model for coastal and estuarine flows and it is based on the general-purpose finite element partial differential equation (PDE) solver *Firedrake* (Rathgeber et al., 2016; Kärnä et al., 2018). It has been employed for several studies on the feasibility and optimisation of tidal energy (Angeloudis et al., 2018; Goss et al., 2020; Harcourt et al., 2019). In this particular study we solve the non-conservative form of the nonlinear shallow-water equations in two-dimensions,

$$\frac{\partial \eta}{\partial t} + \nabla \cdot (H_d \mathbf{u}) = 0, \tag{1}$$

$$\frac{\partial \mathbf{u}}{\partial t} + \mathbf{u} \cdot \nabla \mathbf{u} + g \nabla \eta = \nabla \cdot \left( \nu (\nabla \mathbf{u} + \nabla \mathbf{u}^T) \right) - \frac{\boldsymbol{\tau_b}}{\rho H_d} - \frac{c_t}{\rho H} |\mathbf{u}| \, \mathbf{u} + f \mathbf{u}^{\perp}, \tag{2}$$

where $\eta$ is the water elevation, $H_d$ is the total water depth, $\mathbf{u}$ is the depth-averaged velocity vector, and $\nu$ is the kinematic viscosity of the fluid. The term $f\mathbf{u}^{\perp}$ represents the Coriolis "force", $\mathbf{u}^{\perp}$, included in non-idealised cases, is the velocity vector rotated counter-clockwise

---

[1] `https://floris.readthedocs.io/en/master/index.html`

[2] `http://thetisproject.org/`

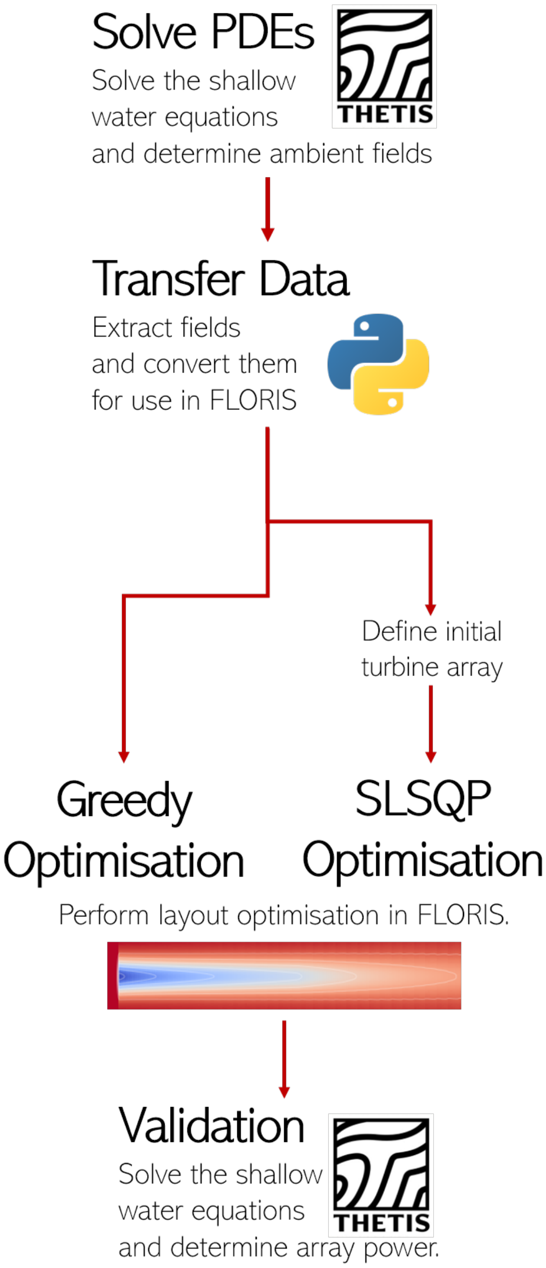

Figure 1: Schematic representation of model coupling and the optimisation sequence.

over 90°, and $f = 2\Omega\sin(\zeta)$ with $\Omega$ the angular frequency of the Earth's rotation and $\zeta$ the latitude. In idealised cases, bed shear-stress ($\tau_b$) effects are represented through a quadratic drag formulation,

$$\frac{\boldsymbol{\tau_b}}{\rho} = C_D|\mathbf{u}|\mathbf{u}. \tag{3}$$

For practical simulations undertaken in this work the Manning's $n_M$ formulation applied is given as,

$$\frac{\boldsymbol{\tau_b}}{\rho} = g n_M^2 \frac{|\mathbf{u}|\mathbf{u}}{H_d^{\frac{1}{3}}}, \tag{4}$$

which is used instead, following Mackie et al. (2021). Additionally and when relevant, intertidal processes are treated using the wetting and drying formulation of Karna et al. (2011). The shallow-water equation is discretised using the discontinuous Galerkin finite element method (DG-FEM) whereas the semi-implicit Crank-Nicolson scheme is employed for time-marching the solution. The resulting discrete system of equations is then solved iteratively with the Newton's method available in PETSc (Balay et al., 2016). Finally, $c_t$ is an additional parameterisation used to represent the turbines' thrust as described in the following section.

### 2.2. *Discrete turbine representation in Thetis*

Turbine rotors are represented in *Thetis* by areas of increased bed friction by adopting the linear momentum actuator disc theory (Kramer and Piggott, 2016). In the 2D depth-averaged form of the shallow-water equations, the force as a result of an array of turbines is:

$$F_{\text{array}} = \int_{\Omega_{\text{array}}} \rho\, c_t(\mathbf{x})\ |\mathbf{u}(\mathbf{x})|\ \mathbf{u}(\mathbf{x})\,\mathrm{d}\mathbf{x}, \tag{5}$$

where $c_t(\mathbf{x})$ is a thrust coefficient function given as:

$$c_t(\mathbf{x}) = \frac{1}{2} C_t(\mathbf{u}(\mathbf{x}))\, A_t\, d(\mathbf{x}), \tag{6}$$

where $A_t$ is the turbine swept area, $C_t$ is the thrust coefficient as a function of the velocity $\mathbf{u}(\mathbf{x})$, and $d(\mathbf{x})$ is the local turbine density. The turbine density $d(\mathbf{x})$ is constructed using a vector $\mathbf{m}$ comprising the coordinates of turbines within the array. This discrete turbine representation employs the exponential bump function as in Funke et al. (2014), which in 1-D takes the form

$$\psi_{p,r}(x) \equiv \begin{cases} e^{1-1/\left(1-\left|\left|\frac{x-p}{r}\right|\right|^2\right)} & \text{for } \left|\left|\frac{x-p}{r}\right|\right| < 1 \\ 0 & \text{otherwise} \end{cases}, \tag{7}$$

where $r$ is the radius of the bump. Equation (7) is employed in defining the turbine density $d_i$ for a turbine $i$ at a position $m_i = (x_i, y_i)$ as the normalised product of 1-D bump functions:

$$d_i(\mathbf{x}) = \frac{\psi_{x_i,r}(x)\psi_{y_i,r}(y)}{\Xi\ r^2}, \tag{8}$$

where $\Xi = \int_{-1}^{1}\int_{-1}^{1} e^{\left(\frac{-1}{1-x^2} - \frac{1}{1-y^2} + 2\right)}\,\mathrm{d}x\,\mathrm{d}y \approx 1.45661$ is the integral of the bump function in the case $r = 1$. The aggregate of the individual turbine densities $d_i$ provides the overall $d(\mathbf{x})$ function:

$$d(\mathbf{x}) = \sum_{i=1}^{N} d_i(\mathbf{x}), \tag{9}$$

where $N$ is the number of turbines deployed.

Following the notation of (5), the power extracted at any given moment by the array can be approximated as

$$P_{\text{array}} = \int_{\Omega_{\text{array}}} \rho\, c_p(\mathbf{x})\, |\mathbf{u}(\mathbf{x})|^3 \, \mathrm{d}\mathbf{x}, \tag{10}$$

where $c_p(x)$ is a power coefficient function given as

$$c_p(\mathbf{x}) = \frac{1}{2} C_p(\mathbf{u}(\mathbf{x})) A_t d(\mathbf{x}), \tag{11}$$

where $C_p$ is a power coefficient which we assume is related to the thrust coefficient through the formulation (Martin-Short et al., 2015)

$$C_p(\mathbf{u}(\mathbf{x})) = \frac{1}{2}\left(1 + \sqrt{1 - C_t(|\mathbf{u}(\mathbf{x})|)}\right) C_t(|\mathbf{u}(\mathbf{x})|). \tag{12}$$

In equations (5) and (10) it is assumed that the ambient velocity is the same as the 'through-turbine' local velocity, $\mathbf{u}(\mathbf{x})$, (i.e. the velocity once the turbine is operating). This is a reasonable approximation for relatively coarse meshes with distributed rather than discrete turbine density fields (Schwedes et al., 2017). However, for micro-siting arrays where the thrust force is concentrated at the turbine location, this assumption becomes invalid. In addressing this we adopt the correction for deriving a relationship between free-stream and through-turbine velocities as derived in Kramer and Piggott (2016).

### *2.3. Analytical wake modelling using FLORIS*

*FLORIS* utilises a number of analytical models to predict the mean wake velocities and power output of turbine arrays (NREL, 2020). In the present study, we make use of FLORIS's Gaussian model originally introduced by Bastankhah and Porté-Agel (2014) which computes the normalised velocity deficit via the expression

$$\frac{\Delta U}{U_\infty} = \left(1 - \sqrt{1 - \frac{C_T}{8\left(k^* x/d_0 + \epsilon\right)^2}}\right) \times e^{\left(-\frac{1}{2(k^* x/d_0+\epsilon)^2}\left\{\left(\frac{z-z_h}{d_0}\right)^2 + \left(\frac{y}{d_0}\right)^2\right\}\right)}, \tag{13}$$

where $U_\infty$ is the approaching streamwise velocity, $z$ is the wall-normal coordinate with $z_h$ the turbine hub height, $k^*$ is the growth rate of the wake $(\partial\sigma/\partial x)$, $d_0$ is the diameter of the wind turbine and $\epsilon$ is the normalised Gaussian velocity deficit at the rotor plane. For our calculations the local wake growth rate $k^*$ is estimated using the local streamwise turbulence intensity, $\mathcal{I}$ (Niayifar and Porté-Agel, 2016). We should note here that the Gaussian velocity model has been selected instead of the more traditionally used Jensen model (Jensen, 1983) which is of similar computational cost but it is known to neglect the wake velocity variation in the cross-flow direction (Dufresne and Wosnik, 2013; Chamorro and Porté-Agel, 2009). Turbine power output on the other hand, is calculated using a power thrust-velocity relationship specified for each individual turbine. This requires a combination model to account for the contributing wake velocity deficit from upstream and other neighbouring turbines. Here, we have selected to use the free-stream linear superposition (FLS) method to account for the cumulative wake effects within the tidal array. The velocity deficit, $\overline{\Delta \mathbf{u}}\,(x, y)$, at a downstream location $(x, y)$ is calculated as,

$$\overline{\Delta \mathbf{u}}(x, y) = \sum_{i=1}^{N} \left(\overline{\Delta \mathbf{u}}_i|_{(x,y)}\right), \tag{14}$$

where $\overline{\Delta \mathbf{u}}_i|_{(x,y)}$ is the contribution the wake of each turbine $i$ at the downstream location $(x, y)$ (Machefaux et al., 2015).

### *2.4. Optimisation approach*

The existing layout optimisation procedure in *FLORIS* (Fleming et al., 2016) is adapted to maximise the average power computed using several input flow fields, rather than the average annual energy production for a single wind rose. The latter is typical of wind farm optimisation and would not apply to tidal-array optimisation. To this end, we approach the tidal-array micro-siting problem by employing an initial *Thetis* simulation of the tidal channel and extract the ambient velocity fields in the allocated array area for a number of times in a tidal cycle. This ambient flow field data is then imported into *FLORIS*. If necessary, an initial (e.g. aligned/staggered) turbine layout is introduced to *FLORIS* and micro-siting is performed using an appropriate optimisation technique subject to spatial constraints, and minimum turbine separation restrictions. Following optimisation in *FLORIS*, the derived turbine layout is tested in *Thetis* to confirm its increased efficiency. A similar approach to optimisation has previously been undertaken to determine wind plant control strategy, with the objective of optimising yaw settings to minimise wake interaction and increase overall farm power (Gebraad et al., 2014). In a deviation from the study of Gebraad et al. (2014) which pioneered the blending of a CFD flow solver with *FLORIS*, we present herein a first attempt to combine *FLORIS* with a shallow-water solver for tidal application.

As we aim to demonstrate a proof-of-concept for the optimisation *approach*, investigations on specific optimisation algorithms are beyond the scope of this work. *FLORIS*' default optimisation is initially performed using the SciPy minimise function for the idealised models (see Section 4), through the SLSQP (Sequential Least SQuares Programming Kraft (1988)) method. The number of iterations for each minimisation problem was limited to the default value of 50. Altering $2N$ variables (i.e. $x$-, $y$- coordinates for $N$ turbines) for each flow field over 50 iterations becomes highly time-consuming as the number of turbines $N$ increases beyond a small array. An increased array size also entails a larger optimisation space, further stressing conventional optimisation. To address the above, a heuristic-based greedy optimisation technique is tested which positions each turbine sequentially. This allows the imposition of constraints which form acceptance criteria, sequentially adding turbines until the desired capacity is installed or until no possible positions for further turbines remain. In addition the proposed alternative approach allows for the rejection of proposed turbine placements based on aspects such as bathymetric gradient forming a basis for non-trivial objective functions. The simplified sequence is indicated in Algorithm 1.

## 3. Turbine specifications and analytical wake calibration

Before outlining the flow scenarios considered for optimisation it is instructive to also present the turbine specifications and calibration process required to adjust the analytical wake model parameters of *FLORIS* so that shallow-water wakes are accurately represented. Starting with the tidal turbines, uniform specifications are applied across all case studies, summarised in Table 1. Additionally, the turbine dimensions, cut-in and rated speeds are based on known parameters for the SIMEC Atlantis 2 MW AR2000 turbine and the SIMEC Atlantis 1.5 MW AR1500 turbine (SIMEC Atlantis Energy, 2020, 2016). Combining equations (10), (11) and (12) allows the determination of the thrust coefficient at rated speed as $C_{t,rated} = 0.516$. This is lower than the value of $C_t = 0.8$ determined in lab-scale experiments (Stallard et al., 2015; Bahaj et al., 2007) thanks to the turbine size and its rated power output. Figure 2 shows the theoretical tailing of the thrust coefficient for higher velocities. This has been approximated by Cardano's formula (Wituła and Słota, 2010) to produce a simpler equation to prevent the need for third-order polynomial inversion that is otherwise required to calculate the power coefficient (and power) at every instance of the hydrodynamic simulation. Below the cut-in

**Algorithm 1** Sequential addition of turbines to domain using greedy optimisation.

*CONDITIONS*: Each turbine must meet a minimum $A$-% average turbine capacity factor, have maximum reduction of power to any other turbine of $B$-% and maximum reduction of power to the sum of individual turbines (that face power output reductions) of $\Gamma$-%.

*CONSTRAINTS* $(\Delta, E)$: Minimum distance constraints for turbine placement, specified in turbine diameters away from considered coordinate.

```
while iteration no. $<$ maximum no. of iterations do
    while no. of turbines $<$ maximum no. of turbines do
        Calculate and add turbine wakes to flow fields over selected tidal cycles.
        Calculate a moving average flow magnitude to deter turbine placements on wake edges.
        Identify coordinate of highest average velocity magnitude as a candidate turbine location.
        Add turbine at candidate site and impose wake on flow field.
        Calculate the average power (using each individual field) for all turbines including the new turbine.
        if CONDITIONS are met then
            Add candidate site to list of accepted coordinates.
            Impose a restriction for turbine placement within a limiting distance $\Delta$ around new coordinate.
        else
            Add candidate site to list of blocked coordinates.
            Impose a restriction for turbine placement within a limiting distance of $E$ around blocked coordinate.
        end if
    end while
end while
```

speed, the thrust coefficient is ramped up exponentially to prevent discontinuities which may cause instabilities within the hydrodynamic model without affecting the total power produced. For consistency, thrust and power coefficients are applied uniformly for both models, with the resultant power curve illustrated in Figure 2.

Table 1: Common input parameters.

| | |
|---|---|
| Fluid density, $\rho$ | 1025 kg/m$^3$ |
| Rotor swept diameter, $D$ | 20 m |
| Hub height, $z_{\text{hub}}$ | 18 m |
| Turbine cut-in speed, $u_{\text{in}}$ | 1 m/s |
| Turbine rated speed, $u_{\text{rated}}$ | 3.05 m/s |

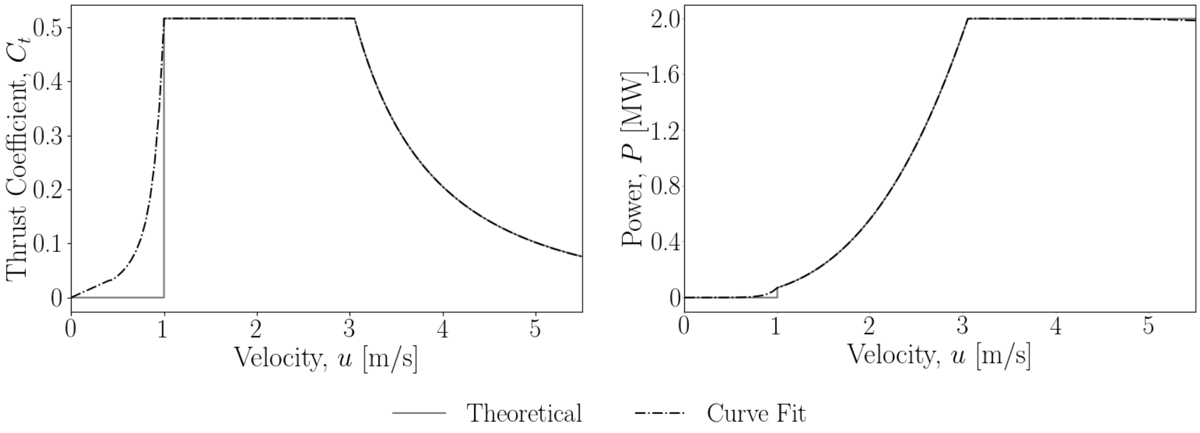

Figure 2: Left: Thrust coefficient function combining the tailing approximated by Cardano's formula relative to theoretical thrust coefficients for a 2 MW turbine. Right: corresponding power curves.

### *3.1. FLORIS-specific inputs*

As we apply *FLORIS* in the tidal-energy "domain", a number of *FLORIS*-specific parameters need to be altered to match appropriate values for a tidal setting (Table 2).

Table 2: *FLORIS* input parameters.

| | |
|---|---|
| Flow shear power law exponent | 0 |
| Flow veer | 0 |
| Axial induction factor exponent | 0.8325 |
| Initial turbulence intensity, $\mathcal{I}_0$ | 12% |
| Ambient turbulence intensity, $\mathcal{I}$ | 20% |

To begin with, the flow shear power law exponent and veer which describe the change in vertical velocity and direction, respectively, are both set to 0, omitting vertical variability to remain consistent with *Thetis*. Additionally, the turbulence model chosen for FLORIS is well-documented in Crespo and Hernández (1996) and the axial induction factor exponent set to the empirically determined value. The initial turbulence intensity at the turbines, $\mathcal{I}_0$, has been determined experimentally at smaller scales to be 12% at the rotor plane for three-blade model tidal turbines (Stallard et al., 2015). Hub height streamwise turbulence intensity has been determined from ADCP deployments upstream of the Meygen Phase 1A turbines to be approximately 10% and 12% for peak flood and ebb flows respectively (Coles et al., 2018). Measured data in the Inner Sound of the Pentland Firth suggests the ambient turbulence intensities at peak flow speeds are 13% and 17% during flood and ebb tides, increasing linearly as the flow speed reduced (Hardwick et al., 2015). As the turbulence intensity is assumed uniform for simplicity, the initial ambient turbulence intensity is estimated to be 20%, as flow speeds (for optimisation purposes) will typically range from 2–5.5 m/s.

### 3.2. Calibration of FLORIS wake effects

Wake-specific parameters are also calibrated here to replicate the velocity deficits exhibited by *Thetis*. These include $k_a$ and $k_b$, parameters that relate to turbulence intensity and wake width. These combine and determine the value of the wake growth rate, $k^*$, which eventually enters the Gaussian velocity deficit equation (13) calculated as,

$$k^* = k_a \cdot \mathcal{I} + k_b. \tag{15}$$

The second set of parameters $\alpha$ and $\beta$ are used for the quantity, $x_0$, which defines the onset of the far wake,

$$x_0 = D\frac{1+\sqrt{1-C_t}}{\sqrt{2}\left(4\alpha \cdot \mathcal{I} + 2\beta\left(1-\sqrt{1-C_t}\right)\right)}. \tag{16}$$

Calibration is performed using differential evolution (as implemented within SciPy's optimisation library (Virtanen et al., 2020)) to optimise the wake parameters $k_a$, $k_b$, $\alpha$ and $\beta$ such that the r.m.s. error between wakes in *Thetis* and *FLORIS* is minimised. Calibration is performed for $u_{\text{rated}}$ only, and then compared to calibrations for speeds below and above rated to verify the primary calibration. An idealised model consisting of a single turbine in the channel described in Section 4.1 is used to create a velocity deficit to be investigated over 20 diameters downstream for this purpose.

The results of this calibration are shown in Table 3, with the r.m.s. error between *Thetis* and *FLORIS* fields below 0.6% in the area of interest from 1.5–20$D$ downstream. The difference in turbine representation is presented in Figure 3, clearly showing higher values of the *FLORIS* flow field velocity compared to *Thetis* as the velocity reduces approaching the bump function that represents the presence of the device. Immediately downstream of the *FLORIS* turbine, the velocity is lower than in *Thetis* due to the greater deficit imposed by *FLORIS*, which comes as a result of the discontinuous nature of the analytical wake model at the turbine location. The discrepancy in turbine representation leads to the decision to calibrate based on the flow field from 1.5$D$ downstream in a zone of width 3$D$ to also capture the expansion width of the far wake. It should be noted that this is typically the region of highest error between not only differing turbine representation methods, but also to measured data; existing research has already demonstrated that accurately capturing the wake dynamics may require investigation of several different approaches to turbine modelling (Sandoval et al., 2021). The central region of the wake is well calibrated, with increased r.m.s. error bands on the edges of the wake, though within acceptable margins of at most 1%. At rated speed, this representation is considered acceptable, with a 1% velocity variation on the outer wake unlikely to largely impact optimisation, considering the additional assumptions within these parameterisations.

A comparative analysis of the wake parameters for $u_{\text{rated}}$ against calibrations at lower and higher flow speeds (Table 4) demonstrates that the overall r.m.s. error of these wake parameters

Table 3: Calibrated wake parameters for Gaussian model.

| | |
|---|---|
| $k_a$ | 0.1087 |
| $k_b$ | 0.006912 |
| $\alpha$ | 0.4886 |
| $\beta$ | 0.2496 |

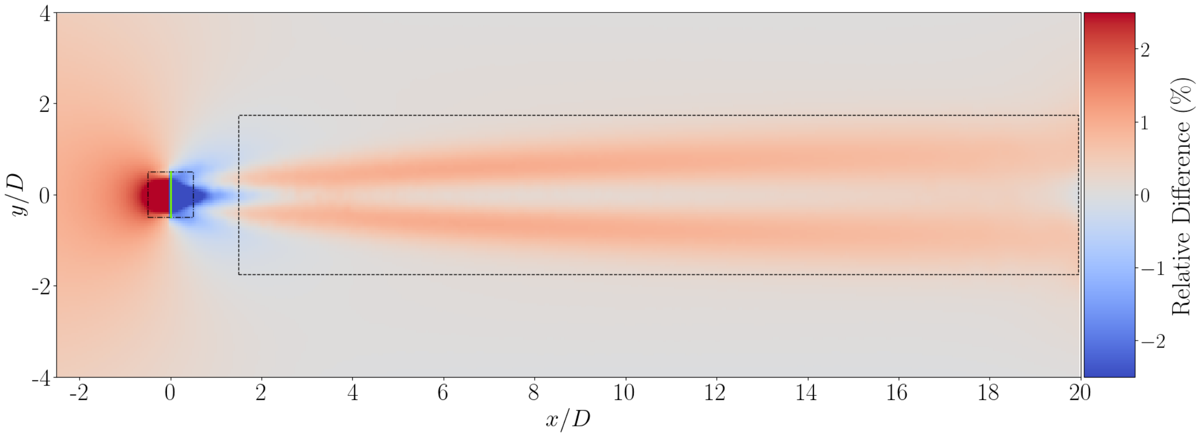

Figure 3: Relative difference between *Thetis* and *FLORIS* flow fields with positive magnitude (red) representing a higher *FLORIS* estimation of velocity. The area indicated by a black square on the left shows *Thetis* area of increased friction whilst solid green line shows *FLORIS* turbine. Black box on the right defines area over which r.m.s. error is calculated for calibration at $u_{\text{rated}}$ alone, see Table 4.

is still acceptable as the analytical wake model is tested within its expected range. With decreasing velocity, the wake width increases and as the velocity approaches cut-in speed the immediate wake width begins to exceed the turbine diameter, increasing the r.m.s. error, albeit within acceptable levels.

Table 4: Comparison of the r.m.s. error between *Thetis* and *FLORIS* flow fields for calibration at rated speed alone vs. direct calibration at the velocity specified.

| Velocity, $u$ (m/s) | r.m.s. error (%) | |
|---|---|---|
| | Rated Speed Calibration | Direct Velocity Calibration |
| 1.5 | 1.243 | 0.379 |
| 2.5 | 0.756 | 0.325 |
| 3.25 | 0.575 | - |
| 4.5 | 0.130 | 0.099 |

For completeness we present the results of a separate calibration performed between the analytical wake model and flume data, which capture the full three-dimensional wake turbulence dynamics that are not captured within 2D depth-averaged models. A comparison between the different wake behaviour and the respective *FLORIS* calibrated solutions are shown in Figure 4. Specifically, Figure 4 shows

- *Thetis* vs Thetis-calibrated *FLORIS* depth-averaged wake profiles;
- Stallard et al. (2013) data vs Stallard-calibrated *FLORIS* prediction for an isolated turbine at hub-height $z_{\text{hub}}$.

Froude-scaling has been applied for comparison against laboratory data (Stallard et al., 2013). Calibration to this data shows excellent agreement beyond $\approx 3D$–$3.5D$ and therefore the potential to calibrate to 3D data.

Even here however, the analytical representation of the near wake could be improved. This further highlights the challenge of calibration between *Thetis* and *FLORIS* as even on the depth-averaged profile, the immediate deficit downstream of the turbine is substantially greater relative to *Thetis*. Nevertheless, the *Thetis* calibrated wake has been well-calibrated beyond $1.5D$; since turbines are not to be placed in such close proximities, this is not expected to impact optimisation.

The logic for using the analytical wake models calibrated against the depth-averaged *Thetis* data is in order to make direct evaluation of the *FLORIS* based optimal array designs using *Thetis* meaningful. For real world applications the initial wake calibration step should be conducted against the best possible wake data available, from observations and/or high-resolution CFD.

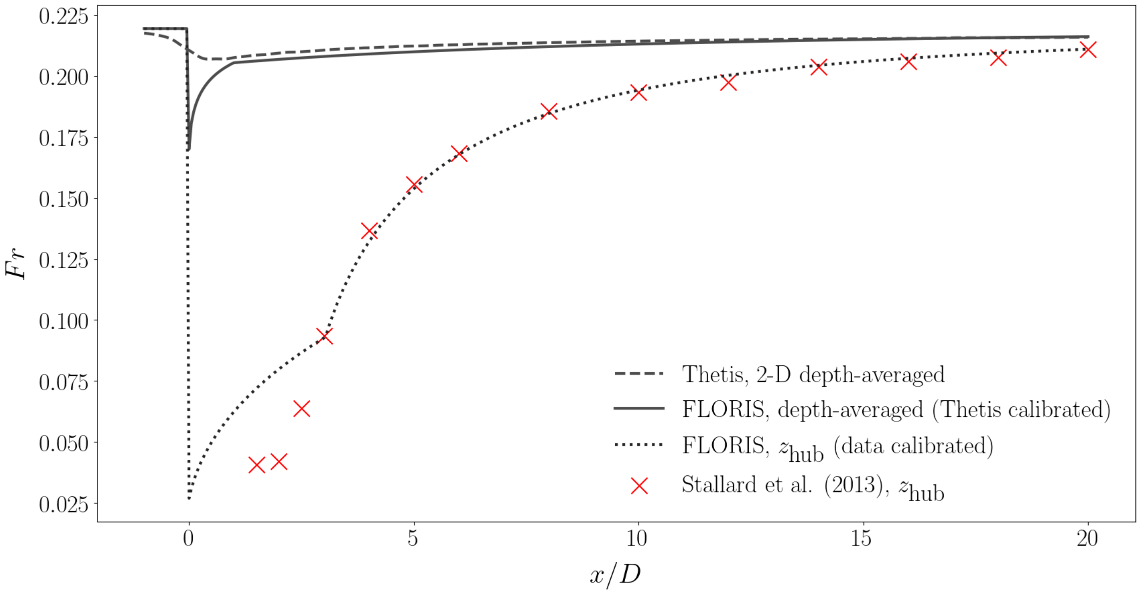

Figure 4: Longitudinal profile for wake Froude number $Fr = \frac{|\mathbf{u}|}{\sqrt{gH_d}}$, both depth-averaged for comparison between calibrated *FLORIS* vs *Thetis* and at hub height ($z_{\text{hub}}$) for comparison between calibrated *FLORIS* vs experimental data of Stallard et al. (2013).

## 4. Case Studies

In demonstrating this novel tidal-array optimisation framework, we consider models of increasing complexity. First, we consider the micro-siting of an initially dense $2 \times 4$ array with three rotor diameter ($3D$) spacing between turbines both transversely and longitudinally which is situated within an idealised channel with and without a headland. These imitate two examples from Funke et al. (2014) and serve in validating the performance of the current approach prior to assessing a more realistic full-scale optimisation problem. For our realistic flow problem we consider the Pentland Firth region with an array size of $4 \times 6$ turbines and a spacing of $5D$ between them in both directions. Both idealised and realistic cases are illustrated in Figures 5 and 6, respectively, together with the computational meshes used by *Thetis* for the hydrodynamic simulations. In all cases, the mesh generation process employs the open-source code *qmesh* (Avdis et al., 2018), featuring a 3 m element resolution for the idealised cases, and 5 m for the Pentland Firth case within the allocated tidal array. This element size was selected using a mesh sensitivity study on the wake resolution confirming the mesh resolution independence of the results within the array. For the optimisation problem we have imposed a number of spatial conditions/constraints. The "greedy" optimisation approach features a minimum of three diameters ($3D$) distance separating each turbine and a blocked radius of one diameter ($1D$) for each "failed iteration" ($\mathit{\Delta} = 3D$, $E = 1D$), which we apply across all considered cases. The $3D$ separation constraint between turbines is applied for all optimisation techniques to prevent the potential for extreme flow deficits behind closely spaced transverse turbines (typically $1.5D$–$5D$ for tidal turbines (Stallard et al., 2013)). Moreover, turbine coordinates are limited to not lie within $D/2$ of the array boundaries defined in *Thetis* so that turbines do not overlap/exceed the specified boundary limits. The minimum power requirements are specified as a minimum 17.5% capacity factor per turbine, a 4–5% maximum reduction of power for individual turbines and a 8–9% maximum reduction in the cumulative power of the particular turbines that face a power reduction, varying slightly between cases ($A = 17.5\%$, $B =$ 4–5%, $\mathit{\Gamma} =$ 8–9%). Specific details for each case study are expanded below.

### *4.1. Steady-state flow through an idealised channel*

An idealised channel of dimension (640 × 320) m featuring a (320 × 160) m region where a tidal array is to be deployed, provides sufficient space to tightly pack turbines across the width of the channel, but is short enough to prevent substantial wake recovery. The bathymetry is consistent across the full domain at 50 m depth. Eddy viscosity is set to a constant value of $1\,\mathrm{m}^2/\mathrm{s}$ across the domain away from the boundaries as per previous studies (Vouriot et al., 2019). For simplicity, a quadratic drag coefficient $C_D = 0.0025$ is used, as per previous investigations of the Pentland Firth, e.g. (Draper et al., 2014), which represents a fairly smooth bed. For our assumed steady case herein, the imposed flow is constant and can be represented by a single flow field, which was determined in Thetis with a hyperbolic tangent ramp from an initial equilibrium condition with an inflow velocity, $u = 3.175\,\mathrm{m\,s^{-1}}$ (close to $u_{\mathrm{rated}}$), while imposing a constant elevation of 0 m at the outflow.

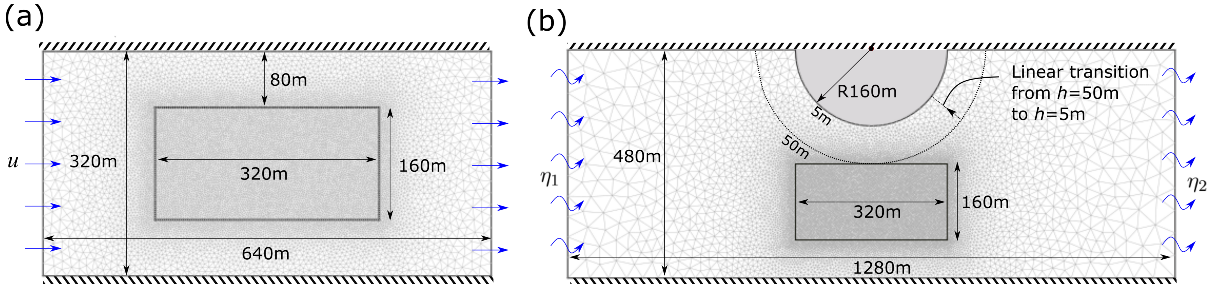

Figure 5: a) Idealised rectangular channel; b) Idealised headland channel indicating bathymetric changes in the proximity of the headland.

### *4.2. Transient flow around an idealised headland channel*

Headlands and islands are key in providing highly energetic channels that make tidal streaming a feasible prospect. Therefore, a simple headland model provides the next step whereby a distinct location of higher energy density exists for turbines to be placed. In this case, the overall channel width and length are increased to 480 m × 1280 m for the headland (represented by 160 m radius semi-circle) to be introduced, where the velocity is greater due to flow conservation with the constriction from 480 m to 320 m acting in a similar manner as a Venturi flume, accelerating the flow. A bathymetric gradient is applied radially, with the depth reduced gradually from 50 m for the overall domain to 5 m along the headland, imitating a shore. Simple harmonic signals are defined (Eq. 17, Eq. 18) to drive the oscillatory flow to verify *FLORIS*' capability to optimise for multiple fields of data. The following equations

$$\eta_1 = A_{\text{tide}} \cdot \sin\left(\frac{2\pi t}{T}\right), \tag{17}$$

$$\eta_2 = -A_{\text{tide}} \cdot \sin\left(\frac{2\pi t}{T}\right), \tag{18}$$

provide the assigned local elevation $\eta_1, \eta_2$, at each of the boundaries and are signals of equal magnitude and opposite direction. Here, $A_{\text{tide}}$ is the tidal amplitude, $t$ is the simulation time and $T$ is the tidal period. Values of $T = 1\,\text{h}$, and $A_{\text{tide}} = 0.275\,\text{m}$, deliver a velocity profile with a peak magnitude close to the rated velocity of current tidal devices (i.e. 2.5–3 m/s). Following a spin-up time of 1.5 hours, fields exported for optimisation are between the cut-in and maximum speeds, over a single tidal cycle.

### *4.3. Application to the Pentland Firth, Scotland, UK*

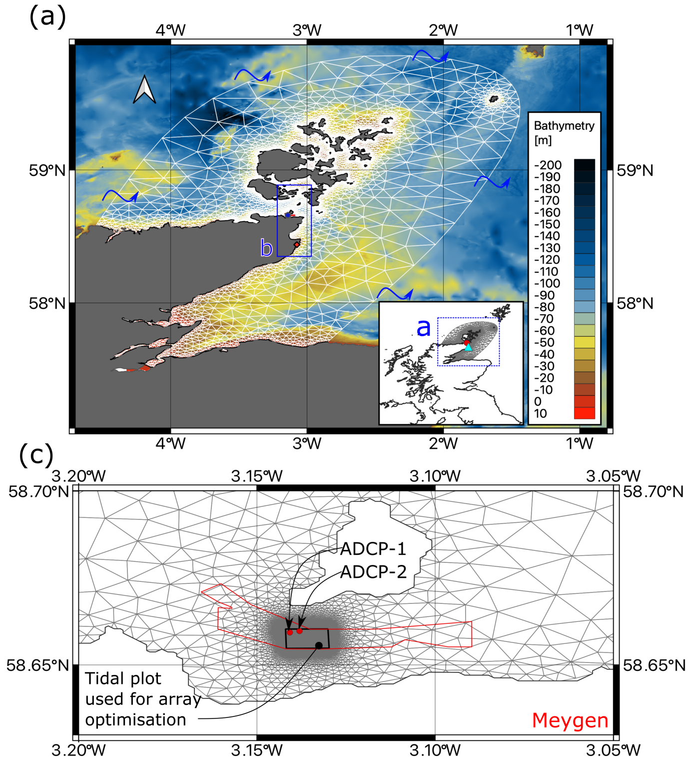

Figure 6: Computational domain for the Pentland Firth case study. a) Domain extents and Marine Digimap bathymetry dataset Edina Digimap Service (2020) interpolated to elements; b) close-up to island scale; c) close-up to channel scale. The tide gauge and ADCP locations used to calibrate the model are also indicated, alongside the tidal array deployment zone considered for array optimisation.

The Orkney archipelagos in north Scotland, UK (Figure 6) features sites characterised by high tidal energy levels. This is especially pronounced in the area of Pentland Firth, a strait separating mainland Scotland from the Orkney Islands. There, flow speeds regularly exceed $5\,\mathrm{m\,s^{-1}}$ (Draper et al., 2014) and thus the Inner Sound of the Pentland Firth is a prime site for tidal array deployment as discussed by several studies investigating the energy resource (Adcock et al., 2013; Draper et al., 2014; O'Hara Murray and Gallego, 2017), potential environmental impacts (Martin-Short et al., 2015) as well as the micro-siting of turbines within arrays (Funke et al., 2014). Within that location is the Meygen site, where a subset of a larger array has already been deployed.

The regional hydrodynamic model shown in Fig. 6a makes use of one arc-second resolution bathymetry, acquired from Edina Digimap Service (Edina Digimap Service, 2020). Open boundaries are tidally forced using eight tidal constituents (Q1, O1, P1, K1, N2, M2, S2, K2) derived from TPXO (Egbert and Erofeeva, 2002). The model, subjected to 2 days of spin-up time, hindcasts 32 days from 01/08/2017 to 01/09/2017. This timeframe is selected according to the availability of ADCP data (Coles et al., 2018), spanning sufficient duration to resolve the principal constituents driving the flow (i.e. M2 and S2). Over this period, predictions are simultaneously compared against UK Hydrographic Office data recorded at a tide gauge located at Wick (Table 5).

Table 5: Comparison between observed and predicted values of principal tide constituents M2 and S2 at Wick tide gauge and ADCP locations.

| Location | Constituent | Amplitude $\alpha$ (m) | | Phase $\phi$ (°) | |
|---|---|---|---|---|---|
| | | Observed | Predicted | Observed | Predicted |
| Wick | M2 | 1.02 | 1.03 | 322.30 | 322.45 |
| | S2 | 0.35 | 0.37 | 0.30 | 359.56 |
| ADCP-1 | M2 | 2.59 | 2.86 | 239.90 | 236.94 |
| | S2 | 1.02 | 1.12 | 278.22 | 293.60 |
| ADCP-2 | M2 | 2.66 | 2.66 | 235.90 | 237.07 |
| | S2 | 0.92 | 0.97 | 237.07 | 300.47 |

The Pentland Firth and Orkney Isles model for our optimisation study has an element size ($\wedge h$) ranging between 300–1,500 m near-shore subject to proximity to the Meygen tidal site or certain island features. This resolution gradually increases to 20,000 m towards the open seaward boundaries. Increased refinement of a uniform element size $\wedge h = 5\,\mathrm{m}$ has been imposed to resolve individual turbines within the Meygen tidal site. The simulation results are produced using a variable Manning's $n_M$ across the domain based on bed classification data provided by the British Geological Survey, as described by Mackie et al. (2021), and a timestep $\Delta t = 100\,\mathrm{s}$.

Model calibration is more sensitive against measured velocity rather than elevation data. Velocity comparisons were established against observed data of at the locations of ADCP-1 and ADCP-2 (Figure 6). In Figure 7 a misalignment can be observed in ADCP-1 during flood tide. This is attributed to several modelling decisions, such as the coarse model resolution surrounding the Meygen site and the rest of the computational domain. In addition, the relatively low resolution of the available bathymetric dataset used in the vicinity is also influential. Nevertheless, the overall model accuracy is deemed appropriate for demonstrating the optimisation method within a practical scenario, acknowledging that these deviations between observational and model data would render further field observation and analysis essential to characterise the local dynamics more accurately. In terms of water elevation predictions, results agree well (Figure 8) with observed values at Wick. There, correlation among observed and predicted water elevation data is approximately 0.982, while the root- mean-square (r.m.s.) error is equal to 0.11 m.

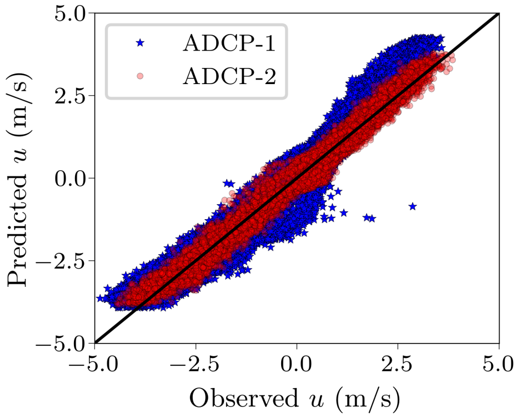
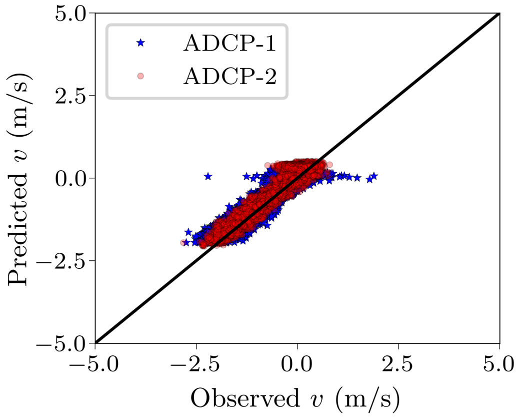

Figure 7: Left: Correlation between observed and predicted $u$-velocity at Pentland Firth monitoring station ($R^2 = 0.93$ and $R^2 = 0.98$ for ADCP-1 and ADCP-2, respectively). Right: Correlation between the observed and predicted $v$-velocity ($R^2 = 0.95$ and $R^2 = 0.84$ for ADCP-1 and ADCP-2, respectively).ADCP data provided by SIMEC Atlantis Energy with further details in Coles et al. (2018)

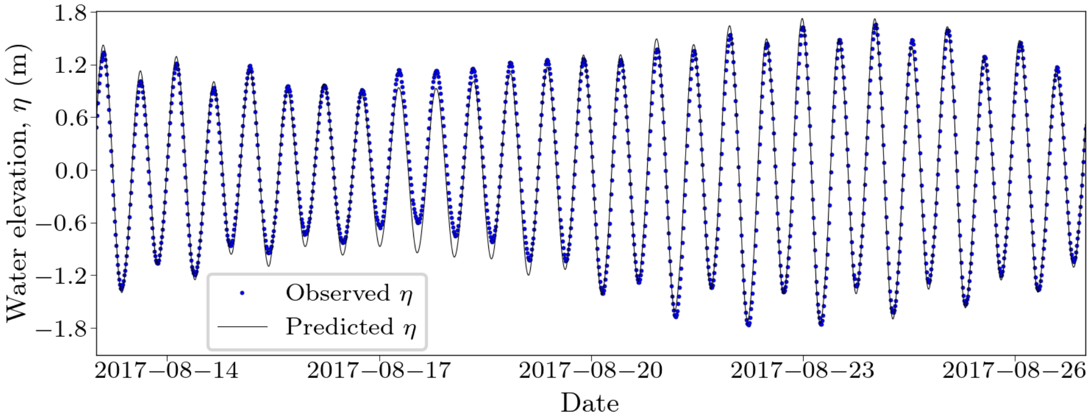

Figure 8: Water elevation at the Wick tide gauge from 13/08/2017 till 27/08/2017. *Thetis* predictions (continuous line) are compared against observed water elevation obtained (circles) with $R^2 = 0.982$ and r.m.s. error = 0.11 m.

Table 6: Results of optimisation methodology applied to each case. The average power $P$ calculated based on testing layouts in *Thetis*.

| Case | Initial Layout | Optimisation Technique | No. of Frames | Average Power, $P$ (MW) | Run Time[3], $t$ (minutes) |
|---|---|---|---|---|---|
| Channel | Aligned | - | - | 13.54 | - |
| Channel | Staggered | - | - | 15.85 (+17.0%) | - |
| Channel | Aligned | *FLORIS* (SLSQP) | 1 | 15.99 (+18.1%) | 0.5 |
| Channel | - | *FLORIS* (Greedy) | 1 | 15.98 (+18.0%) | 0.2 |
| Channel | Aligned | Adjoint (SLSQP) | N/A | 16.00 (+18.2%) | 53.8 |
| Headland | Aligned | - | - | 4.35 | - |
| Headland | Staggered | - | - | 5.44 (+25.2%) | - |
| Headland | Aligned | *FLORIS* (SLSQP) | 6 | 5.61 (+29.0%) | 196.4 |
| Headland | - | *FLORIS* (Greedy) | 6 | 5.53 (+27.4%) | 0.3 |
| Pentland Firth | Aligned | - | - | 20.47 | - |
| Pentland Firth | Staggered | - | - | 20.55 (+0.4%) | - |
| Pentland Firth | Aligned | *FLORIS* (SLSQP) | 18 | 21.72 (+6.1%) | 4002.0 |
| Pentland Firth | - | *FLORIS* (Greedy) | 18 | 23.01 (+12.4%) | 0.8 |

## 5. Optimisation Results

### 5.1. Steady-state flow through an idealised channel

The maximum power possible from the setup of eight 2 MW turbines would be approximately 16 MW based on Figure 2. An aligned turbine placement (Figure 9a) yields power of > 15% below the maximum extractable power, despite the flow speed exceeding $u_{\text{rated}} = 3.175\,\text{m}\,\text{s}^{-1}$. Placing the turbines in the staggered arrangement of Figure 9a leads to improved power output as anticipated, slightly below the maximum achievable.

Optimisation in Floris using SLSQP to maximise power leads to a distribution of turbines across the channel width at varying longitudinal positions subject to separation constraints. Using the greedy approach provides a similar result, with turbines again placed to avoid wake interaction whilst at varying longitudinal positions. The SLSQP approach performed best in completing optimisation due to the simplicity of the input whilst the greedy approach took 2.5 × less time.

An adjoint-based tidal farm optimisation (Funke et al., 2014) conducted within Thetis for the same channel provides similar distributions of turbines across the channel of varying longitudinal distance as in Figure 9, but with placement that appears to exploit the duct effect. This results in maximum power obtained across all approaches (confirmed in Thetis) as optimisation using *Thetis*'s adjoint negates issues in variation of turbine representation, whilst also capitalising on beneficial hydrodynamic effects. The adjoint/gradient-based method was anticipated to be more effective in this case for the above reasons, particularly around (or below) rated speed, whereby the velocity deficits can bring the through-turbine flow velocity below rated and reduce the power produced. Nevertheless, despite different layouts, the power performance is near identical suggesting that multiple solutions achieve the criterion of maximising power output, but with the adjoint taking significantly longer than the greedy approach.

### 5.2. Transient flow around an idealised headland

The idealised headland case considers oscillatory flow to demonstrate optimisation features over unsteady conditions. Three flow fields from each flood and ebb tide are exported. For each of these sets, one is at peak velocity magnitude and two between cut-in and rated speeds. As flow direction and magnitude does not vary significantly, the total of six flow 'frames' performs sufficiently for optimisation in this case, with more frames delivering negligible benefit. Velocity contours for the peak flood flow without turbines are shown in Figure 10 with layouts of different headland cases of Table 6 superimposed. As the flow develops around the headland, the combination of the *vena contracta* effect and the bathymetric gradient contribute to a velocity acceleration that diminishes away from the headland constriction. This provides radial bands of higher energy potential for turbine placement, with only the regions closest to the headland allowing maximum power production at peak flow speeds.

*FLORIS*'s SLSQP based optimisation leads to placement of three turbines within these first two bands (i.e. in flow greater than $3\,\text{m}\,\text{s}^{-1}$), with the remainder of the turbines spread across the width of the channel avoiding wake interaction in a similar manner to the first case. Meanwhile, greedy optimisation places the first turbine in the centre of the first band, subsequently leading to lower power production for the surrounding turbines, which can not be placed as closely within the first two bands due to the separation constraint.

The average power produced by the greedy optimisation array after only 20 iterations exceeds the staggered arrangement (Table 6, Headland & Staggered case), which itself performs particularly well due to the flow direction. However, the greedy optimisation technique leads

---

[3] All simulations were run on a single core. Specification: Intel (R) Xeon (R) Gold 5118 CPU 2.30GHz.

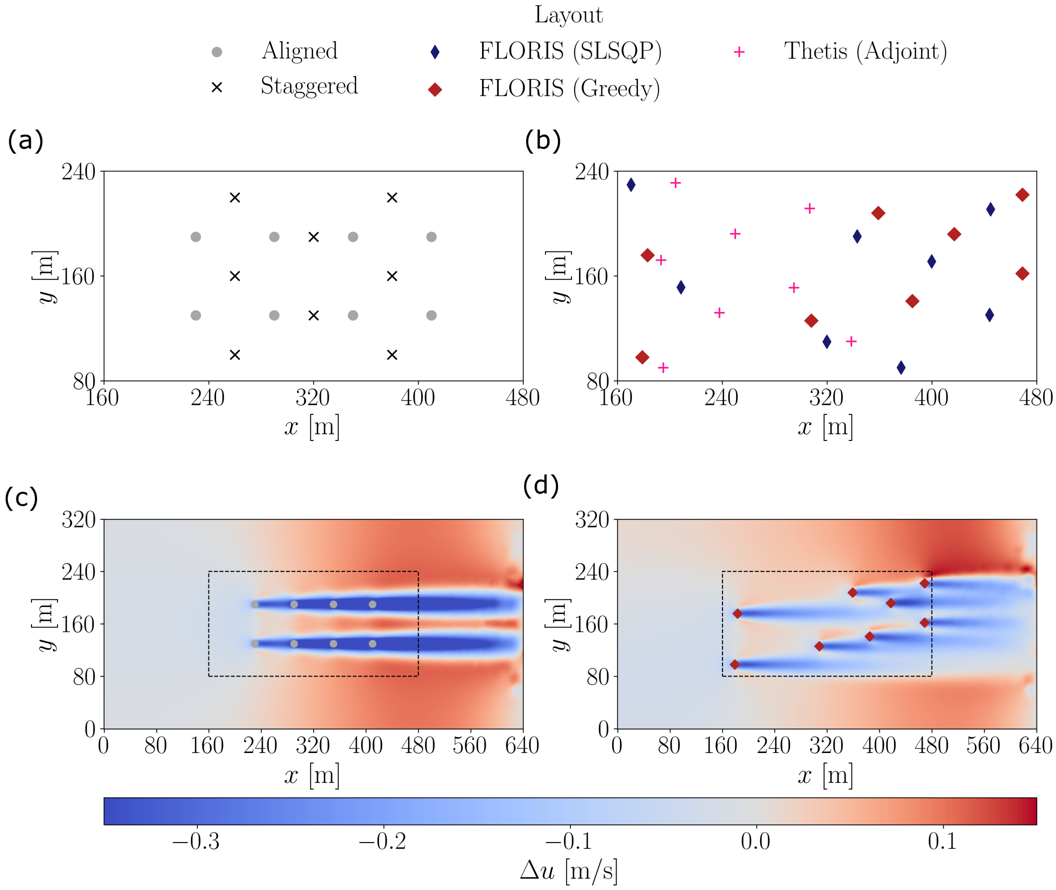

Figure 9: Layouts and *Thetis* predicted velocity deficits ($\Delta u$) for rectangular steady-state idealised channel flow. a) standard (i.e. unoptimised) layouts; b) optimised layouts; c) aligned layout $\Delta u$; d) greedy optimisation layout $\Delta u$.

to 1.8% lower average power than SLSQP, although it does require almost a thousandth of the computational time. Given the time taken for a steady state channel optimisation, the reduction in computational time becomes particularly appreciable compared to adjoint optimisation, which has not been explored further in this work for unsteady cases.

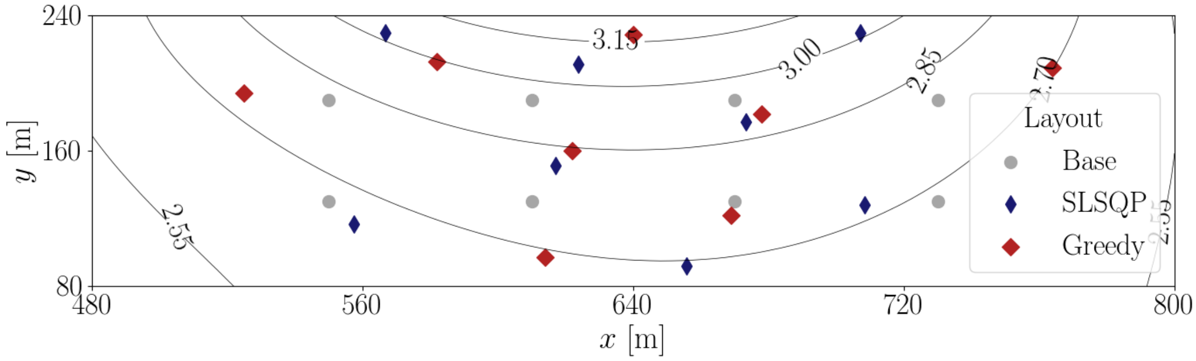

Figure 10: Optimised layouts overlaid on velocity contours for peak flow within the idealised headland channel.

### *5.3. Application to the Pentland Firth, Scotland, UK*

Using three frames from each flood and ebb tide for spring, intermediate and neap cycles, optimisation successfully increased power relative to the aligned case by 12.4% over a month's period (Table 6). The importance of using frames representing both a full tidal cycle as well as a monthly cycle is demonstrated by Figure 13. Optimisation is less effective during flood flows; and even less so during the spring tide. This is as a result of the expected deployment of rated turbines that will experience flow velocities noticeably greater than rated speed for a large proportion of the higher flows expected within the allocated plot. As a result, these are predicted to deliver maximum power irrespective of compounded wakes. This would suggest that within this area, not considering structural constraints, it may be worth using turbines of higher rated speeds to fully exploit the potential energy available. Nevertheless, a positive increase in capacity factor from 42.6% to 47.9% is achieved that could have a significant influence on the feasibility of such an installation.

Greedy optimisation achieved this in 27 iterations, taking a little less than a minute, whilst conventional SLSQP optimisation becomes significantly more costly with increased domain size and number of turbines. As Table 6 shows, in a practical case where velocities exceed $u_{\text{rated}}$ and the flow field is more varied and complex largely due to the local bathymetric profile, a staggered arrangement is far less effective than in the idealised cases. With more turbines within the staggered arrangement, the interaction of multiple wakes has a far more profound effect as shown in Figure 12a,c; the variation of flow velocities means that turbines perform better packed into regions of higher potential. This again highlights the sensitivity of optimisation to turbine $u_{\text{rated}}$; when peak flow speeds are high (relative to $u_{\text{rated}}$), the higher potential regions may have lower influence on optimal array design as, despite wake impingement, turbines still operate at their maximum capacity. Figure 11d sees turbines positioned in the highest power density areas, whereby the southern parts of the site are avoided on the grounds of lower flow magnitudes. Notably, beyond the allocated area for turbine deployment, flow speed exceeds $5.5\,\mathrm{m\,s^{-1}}$ towards the island of Stroma (Figure 6). Harnessing the kinetic energy there may be technically challenging due to the shallower bathymetry and sharper bed gradients. In the optimised configurations, few turbines lie within the high velocity deficit region of upstream wakes due to conditions preventing the reduction of individual turbine power. This is particularly critical during neap tide when flow speeds are low enough to place emphasis onto wake interaction, hence the benefit of optimising for several varying tidal cycles.

A key consideration when examining practical cases is the impedance of the flow due to the presence of turbines (array blockage). The change in volumetric flow over a 1-day period is presented in Table 7 to quantify the impact of the turbine drag on the channel flux, as per Coles et al. (2017). Through the array width only, the reduction in volumetric flow remains below 4%, which is not particularly significant for a spring tide and results partially from the low global blockage of the array and the spaced out distribution of turbines to minimise velocity deficits. As the array size and its turbine density is relatively small when compared to the size of the channel, the influence on the Inner Sound is localised suggesting minimal diversion of flow on a regional scale. With increasing array size, the impact of global blockage effects will likely become more critical, particularly considering site-to-site interactions over the entire Pentland Firth and the Orkney Islands (De Dominicis et al., 2018).

Table 7: Change in volume flux with the introduction of the greedy array layout, over transects of the array width and Inner Sound for a Spring cycle. Different transects are used for the ebb, flood and overall volume flux changes to best account for the impact of the array in each case. A negative change represents a decrease in flow through the channel when turbines are introduced.

| Cycle | Volume flux change, $\Delta Q/Q_{\text{amb}}$ (%) | |
|---|---|---|
| | Array Width | Inner Sound |
| Ebb | -3.33 | -0.47 |
| Flood | -3.59 | -0.17 |
| 24 hours | -3.66 | -0.57 |

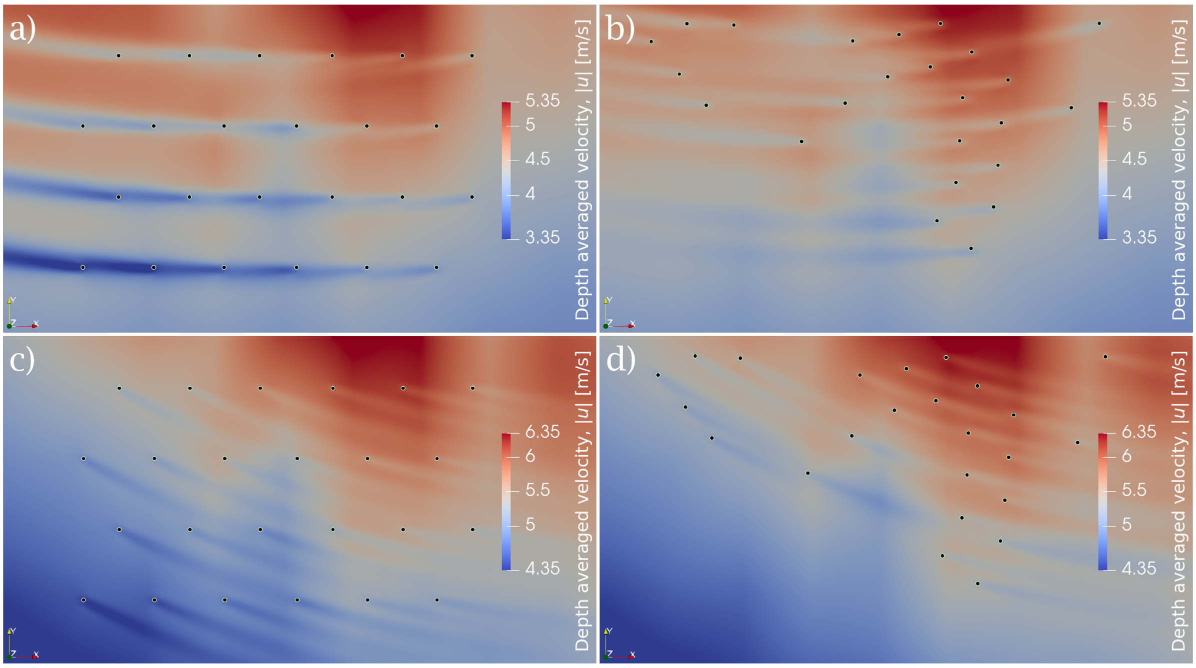

Figure 11: Flood and ebb flow for Pentland Firth case study at peak spring tide computed using the Thetis model with turbine drag simulated. a) staggered arrangement, ebb; b) greedy optimised arrangement, ebb; c) staggered arrangement, flood; b) greedy optimised arrangement, flood.

## 6. Discussion

### *6.1. On the turbine representation and the consideration of local and global blockage*

The general array micro-siting pattern returned by the optimisation approaches (SLSQP and greedy alike) sees turbines positioned within high power density regions and otherwise spread to maintain separation whilst avoiding wake interaction. This also agrees with results reported previously by Stansby and Stallard (2016) that emphasise wake avoidance within the optimisation process.

Under operational conditions below $u_{\text{rated}}$, variation in wake representation can compromise optimisation, as key velocity deficit areas may not be captured accurately. If the wake width is underestimated in the analytical model then downstream turbines could in fact become partially immersed in the upstream wake when evaluated using the hydrodynamic model. This highlights the significance of calibrating wake effects as per Section 3.2. Additional parameters can be considered to improve accuracy, such as varying $\mathcal{I}$ as a function of the flow magnitude, for better agreement against data. These were assumed constant for simplicity in this case. The inclusion of local blockage effects, which has been shown to be possible through ad-hoc corrections in analytical approaches such as *FLORIS* (Branlard and Meyer Forsting, 2020), could also benefit optimisation in high-density, confined scenarios.

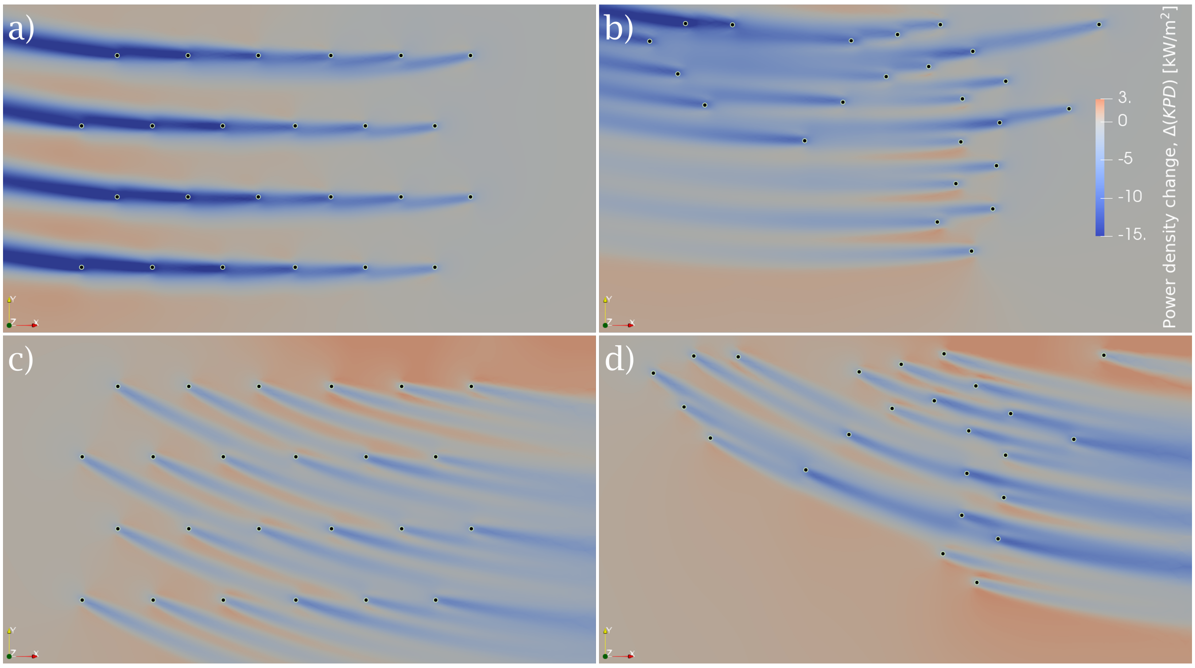

Figure 12: Flood and ebb change in kinetic power density (KPD) for Pentland Firth case study at peak spring tide computed using the Thetis model with turbine drag simulated. a) staggered arrangement, ebb; b) greedy optimised arrangement, ebb; c) staggered arrangement, flood; d) greedy optimised arrangement, flood.

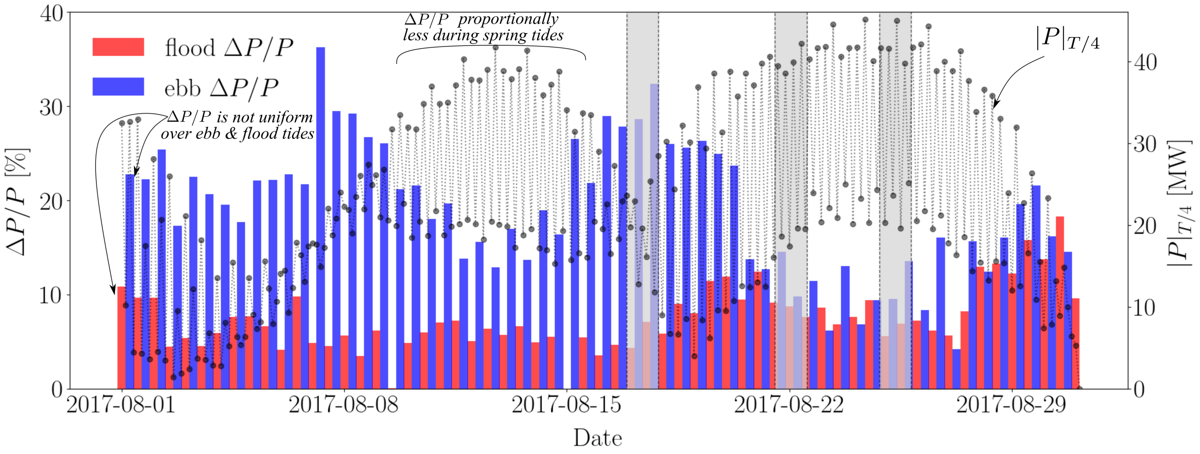

Figure 13: Relative power increase ($\Delta P/P$) comparing greedy to staggered case. Shaded areas indicate periods used to extract ambient flow fields for optimisation. $|P|_{T/4}$ corresponds to the average power in increments of $T/4$.

In the practical case study within the Pentland Firth we consider a turbine array subject to a rating curve, varying flow directionality and including practical clearance constraints. We observe that due to the varying flow direction over ebb and flood tides, blockage becomes challenging to exploit. Considering the flow velocity across the array, we note the persistent exceedance of $u_{\text{rated}}$, across spatial and temporal scales. When velocities regularly exceed $u_{\text{rated}}$, wake effects become locally constrained, and compounded by changes in flow directionality render the duct effect difficult to take advantage of and thus less influential on power production. Based on standard practices, turbines are proposed to be placed in channels where peak flow speeds comfortably exceed $u_{\text{rated}}$. This is due to alternative objectives, such as maintaining a competitive Capacity Factor over the device lifetime. Therefore, if a significant proportion of power is to be extracted above $u_{\text{rated}}$, local blockage and the duct effect becomes tertiary. In addition, during spring tides when $|\mathbf{u}| > u_{\text{rated}}$ over a longer fraction of the tidal cycle, optimal siting of turbines becomes less beneficial in terms of power output.

Furthermore, minimum turbine spacing may likely be forced to exceed $3D$ Ouro et al. (2019) (the value used in this study as the minimum separation constraint), which would again reduce to an extent the positive influence that local blockage may achieve. Nishino and Willden (2013) analytically found that with increasing turbine density in a partial tidal fence, the optimal local blockage will increase for both low and high global blockage cases. The benefit of exploiting blockage effects was demonstrated numerically in Funke et al. (2014) where an adjoint-optimisation approach promoted positioning of idealised turbines (i.e. not subject to a $u_{\text{rated}}$) to form highly dense fence-like structures. However, within the steady-state flow through an idealised channel, the adjoint optimisation in *Thetis*, subject to turbine density limitations ($3D$), delivers negligible gains over our greedy or *FLORIS*'s SLSQP approaches.

A feasible placement of turbines within a channel such as the Pentland Firth is likely to be highly dependent on a number of factors including the bathymetry gradient, bedrock hardness, turbulence loading and a variety of installation and maintenance challenges. The initial turbine density for the Pentland Firth case study was based on an initial separation of $5D$. If the density is increased so that maximum initial separation is reduced to $3D$ (whilst increasing the number of turbines in the initial array), local blockage effects become more prominent, as indicated by the increase in power density around devices in Figure 12. Nevertheless, quantification of the blockage effects by monitoring fluxes and the power density changes over the array (Table 7) suggests that this remains a low blockage case.

### *6.2. On the characterisation of array hydrodynamics*

The optimisation approach described here relies on the use of analytical wake models that typically assume steady-state conditions. Similarly, the hydrodynamics model does not capture horizontal flow structures below the mesh-size scale which means that many unsteady and quasi-steady flow phenomena are not considered in our analysis. This may have implications for the final prediction of the wake deficits and therefore also affect the optimal array layout solution. One phenomenon of relevance which is not captured in our simulations is *dynamic wake meandering*. As turbine wakes interact with the larger tidal-channel turbulent structures, such as near-wall high- and low-speed streaks, near-wake vortices start breaking down giving way to the generation of a cascade of turbulent scales. Additionally, the wake experiences lateral and vertical displacements caused by the larger-scales leading to their significant lateral expansion. These effects are not encapsulated within hydrodynamic models unless the model spatial and temporal resolution is increased and/or combined with more robust turbulence models that capture these effects while avoiding excessive dissipation in the solution. Inherently, all 2-D models are limited in their ability to capture dispersion effects due to the assumed uniform vertical velocity. 3-D shallow-water models on the other hand, can improve the representation of such scales as shown by Stansby (2003) through the addition of a horizontal mixing length scale which alters the velocity profile over the water column, resulting in greater vertical shear; however, further research is required in order to quantify their impact on wake dynamics.

Regarding the global array wake, recent experimental studies on turbulent wakes downstream of a two-dimensional porous obstruction (Zong and Nepf, 2012) shows that the steady wake region increases with increasing porosity whereas the unsteady von Kármán street may be delayed until well beyond the steady wake region. Given the low turbine density, as demonstrated by the global array volume flux (see Table 7), the array's equivalent porosity is small, thus we argue that no further quasi-steady effects are likely to be present in the wake region.

Turbine-scale unsteadiness in the individual turbine's near wake region may be accounted for by a locally modified eddy-viscosity.

An alternative approach for the local and global hydrodynamics may be undertaken using higher-fidelity models such as those that utilise three-dimensional Reynolds-averaged Navier–Stokes (RANS) (Abolghasemi et al., 2016; Deskos et al., 2017) or large-eddy simulation (LES) methods (Churchfield et al., 2013; Ouro et al., 2019) which inherently allow for greater insight and accuracy in the near-wake region by allowing both horizontal and vertical wake dispersion through scale-resolving simulations. Such simulations emphasise how wake avoidance is not only critical for maximum exploitation of the channel potential, but also in reducing turbulence onto downstream turbines which may compromise the devices' lifetime due to fatigue (Thiébaut et al., 2020). Nevertheless, 2-D models are currently the standard option for regional assessments (Coles et al., 2020) and help counteract the computational cost within an optimisation framework. As demonstrated in Section 3.2, and in particular Figure 4, it would be entirely possible to apply the same methodology to a 3-D higher-fidelity either coastal ocean or turbulence-resolving model to acquire greater consistency with measured data.

### *6.3. On the potential applications for large tidal array optimisation*

Whilst a number of optimisation approaches have been proposed for the micro-siting of tidal turbines, these have been limited to idealised setups, or limited control parameters in terms of turbine placement. Some of the more sophisticated methods (e.g. Funke et al. (2016); Culley et al. (2016) that consider blockage effects remain computationally and memory intensive. Taking our practical example of the Pentland Firth, an earlier approach required 24–48 hours on a 64-core supercomputer for a steady state simulation (Funke et al., 2014). Though pioneering, practical constraints including rated turbines, transient tidal flows and realistic bathymetry were not considered in early studies despite having an influence on the interactions between devices and the resource. Similarly, optimisation methods that estimate the objective function gradient iteratively (e.g. SLSQP), quickly become computationally demanding due to the quadratic complexity ($\mathcal{O}(n^2)$) of the optimisation algorithm. The custom greedy approach developed here overcomes these computational constraints and offers a route to also incorporate additional features. These may include cabling constraints (Culley et al., 2016), seabed gradient restrictions, several turbine options and other factors such as wake steering which are considered in the optimisation of offshore wind farm operation (Deskos et al., 2020).

Adjoint-based and greedy methods could be combined in a cyclic manner for optimisation in larger domains whereby a greedy approach acts as a precursor that delivers an initial design to improve upon through adjoint-optimisation. This will sequentially seek to exploit hydrodynamics effects by exploring the parameter space through localised turbine displacements starting from a decent design that should result in the requirement for less optimisation iterations than a pure adjoint-based approach. It many also potentially mitigate the issue of getting stuck in a sub-optimal local optima. Alternatively, given the computational efficiency of the custom greedy optimisation, opportunities can be unlocked to optimise for $N$ turbines at a time in subsets of the turbine deployment area. Turbines introduced can then be included in forward hydrodynamics simulations to account for hydrodynamic impact and blockage effects when designing the rest of the array. Extensions can thus be made towards multi-objective optimisation that balance cost against environmental impacts such as sediment transport or implications for benthic species habitats. This could follow recent work by du Feu et al. (2019).

## 7. Conclusions

A novel optimisation method was demonstrated by retrofitting an analytical wake superposition model, in this case *FLORIS*, for use with a multi-scale coastal hydrodynamics model, *Thetis*.

The method is motivated upon reflection on the bottlenecks observed in existing array optimisation approaches, which depending on acceptable computational costs may be constrained to (a) simplified flow geometries, (b) steady-state flow conditions and (c) idealised turbine representations. The work is driven by the complexity of the array micro-siting problem, where an effective optimisation method should be able to deal with complex flows caused by local bathymetric features and regional coastline, the transient tidal flows over spring neap cycles, and the technical specifications and performance characteristics of the turbine technology that are to be deployed. Once a hydrodynamic model delivers the spatially and temporally varying flow information over a prospective development area, application of a custom greedy placement algorithm within an analytical wake superposition model allows for rapid optimisation.

The methodology was applied to three cases of increasing complexity and was able to demonstrate its potential and highlight multiple considerations emerging as we progress from idealised to practical settings. For a simple steady-state rectangular channel, turbines were arranged in a staggered fashion across the domain, utilising the full width of the domain whilst maintaining $3D$ separation constraints, consistently with alternative optimisation strategies (e.g. SLSQP and adjoint-based optimisation). The headland case demonstrated the capacity to deal with more complicated flows and emphasised the trend of turbines being positioned in areas of higher power density, whilst avoiding wake effects from upstream turbines during ebb and flood flows. The optimisation scenario of 24 turbines in a confined region within the Pentland Firth demonstrated the ineffectiveness of staggered arrangements for non-rectilinear oscillatory flows, and the computationally efficient application of this methodology for complex geometries and flow dynamics. It was found that the resultant method yielded an overall improvement in power output in the order of 12%.

Finally, it was observed that flow asymmetry in conjunction with minimum distance requirements may render the exploitation of local blockage effects rather challenging. The case study using 24 turbines within the Meygen site at the Pentland Firth indicated low levels of global blockage. Given the extensions expected as tidal arrays expand, it is proposed that this approach can be operated iteratively with the hydrodynamic model to account for array-scale blockage as the size of the array is extended.

## Acknowledgements

A. Angeloudis acknowledges the support of the NERC Industrial Innovation fellowship grant NE/R013209/2. D. Coles acknowledges the support of the Tidal Stream Industry Energiser project (TIGER), co-financed by the European Regional Development Fund through the INTERREG France (Channel) England Programme. M. Piggott acknowledges the support of EPSRC under grants EP/M011054/1 and EP/R029423/1. The provision of ADCP data by SIMEC Atlantis Energy is gratefully acknowledged.

## CRediT Statement

**Connor Jordan**: Methodology, Formal Analysis, Investigation, Writing - Original Draft, Writing - Review & Editing, Software, Visualisation. **Davor Dundovic**: Methodology, Formal Analysis, Software, Writing - Review & Editing. **Anastasia Fragkou**: Validation, Writing - Review & Editing. **Georgios Deskos**: Conceptualisation, Software, Writing - Review & Editing. **Daniel Coles**: Data Curation, Writing - Review & Editing. **Matthew Piggott**: Software, Writing - Review & Editing, Supervision. **Athanasios Angeloudis**: Methodology, Software, Investigation, Resources, Writing - Review & Editing, Supervision, Project Administration, Funding Acquisition.

## References

G. Smart, M. Noonan, Tidal Stream and Wave Energy Cost Reduction and Industrial Benefit: Summary Analysis, Technical Report, ORE Catapult, 2018.

M. B. Topper, S. S. Olson, J. D. Roberts, On the benefits of negative hydrodynamic interactions in small tidal energy arrays, Applied Energy 297 (2021) 117091.

U.S. Energy Information Administation, Levelized Cost and Levelized Avoided Cost of New Generation Resources in the Annual Energy Outlook 2020, Technical Report, U.S. Energy Information Administation, 2020.

D. S. Coles, T. Walsh, Mechanisms for reducing the cost of tidal stream energy, 13th European Wave and Tidal Energy Conference (2019).

Z. L. Goss, D. S. Coles, M. D. Piggott, Identifying economically viable tidal sites within the Alderney Race through optimization of levelized cost of energy: Economic viability of the Alderney Race, Philosophical Transactions of the Royal Society A: Mathematical, Physical and Engineering Sciences 378 (2020).

Z. L. Goss, D. S. Coles, S. C. Kramer, M. D. Piggott, Efficient economic optimisation of large-scale tidal stream arrays, Appl. Energy 295 (2021a) 116975.

Z. Goss, D. Coles, M. Piggott, Economic analysis of tidal stream turbine arrays: a review (2021b).

J. F. Chozas, International Levelised Cost of Energy for Ocean Energy Technologies, Technical Report May, Ocean Energy Systems, 2015.

SIMEC Atlantis Energy, Meygen, 2020. URL: https://simecatlantis.com/projects/meygen/.

S. P. Neill, M. R. Hashemi, M. J. Lewis, Optimal phasing of the european tidal stream resource using the greedy algorithm with penalty function, Energy 73 (2014) 997–1006.

P. E. Robins, S. P. Neill, M. J. Lewis, S. L. Ward, Characterising the spatial and temporal variability of the tidal-stream energy resource over the northwest european shelf seas, Applied Energy 147 (2015) 510–522.

S. Funke, P. Farrell, M. Piggott, Tidal turbine array optimisation using the adjoint approach, Renewable Energy 63 (2014) 658–673.

R. Vennell, S. W. Funke, S. Draper, C. Stevens, T. Divett, Designing large arrays of tidal turbines: A synthesis and review, Renewable and Sustainable Energy Reviews 41 (2015) 454–472.

I. Fairley, I. Masters, H. Karunarathna, The cumulative impact of tidal stream turbine arrays on sediment transport in the pentland firth, Renewable Energy 80 (2015) 755–769.

R. du Feu, S. Funke, S. Kramer, J. Hill, M. Piggott, The trade-off between tidal-turbine array yield and environmental impact: A habitat suitability modelling approach, Renewable Energy 143 (2019) 390–403.

S. Nash, N. O'Brien, A. Olbert, M. Hartnett, Modelling the far field hydro-environmental impacts of tidal farms - A focus on tidal regime, inter-tidal zones and flushing, Computers and Geosciences 71 (2014) 20–27.

D. M. Culley, S. W. Funke, S. C. Kramer, M. D. Piggott, Integration of cost modelling within the micro-siting design optimisation of tidal turbine arrays, Renew. Energy 85 (2016) 215–227.

R. du Feu, S. Funke, S. Kramer, D. Culley, J. Hill, B. Halpern, M. Piggott, The trade-off between tidal-turbine array yield and impact on flow: A multi-objective optimisation problem, Renewable Energy 114 (2017) 1247 – 1257.

R. J. du Feu, S. W. Funke, S. C. Kramer, J. Hill, Piggott, The trade-off between tidal-turbine array yield and environmental impact: A habitat suitability modelling approach, Renewable Energy 143 (2019) 390–403.

E. González-Gorbeña, R. Y. Qassim, P. C. Rosman, Multi-dimensional optimisation of Tidal Energy Converters array layouts considering geometric, economic and environmental constraints, Renewable Energy 116 (2018) 647–658.

A. Phoenix, S. Nash, Optimisation of tidal turbine array layouts whilst limiting their hydro-environmental impact, Journal of Ocean Engineering and Marine Energy 5 (2019) 251–266.

R. Vennell, Tuning tidal turbines in-concert to maximise farm efficiency, Journal of Fluid Mechanics 671 (2011) 587–604.

R. Vennell, The energetics of large tidal turbine arrays, Renewable Energy 48 (2012) 210–219.

T. Divett, R. Vennell, C. Stevens, Channel-scale optimisation and tuning of large tidal turbine arrays using LES with adaptive mesh, Renewable Energy 86 (2016) 1394–1405.

S. W. Funke, S. C. Kramer, M. D. Piggott, Design optimisation and resource assessment for tidal-stream renewable energy farms using a new continuous turbine approach, Renewable Energy 99 (2016) 1046–1061.

R. N. King, K. Dykes, P. Graf, P. E. Hamlington, Optimization of wind plant layouts using an adjoint approach, Wind Energy Science 2 (2017) 115–131.

G. L. Barnett, S. W. Funke, M. D. Piggott, Hybrid global-local optimisation algorithms for the layout design of tidal turbine arrays, 2014. arXiv:1410.2476.

T. Nishino, R. H. Willden, Effects of 3-D channel blockage and turbulent wake mixing on the limit of power extraction by tidal turbines, International Journal of Heat and Fluid Flow 37 (2012) 123–135.

L. Chen, P. A. Bonar, C. R. Vogel, T. A. Adcock, Local blockage effects for idealised turbines in tidal channels, Proceedings of the International Conference on Offshore Mechanics and Arctic Engineering - OMAE 10 (2019) 1–10.

P. Stansby, T. Stallard, Fast optimisation of tidal stream turbine positions for power generation in small arrays with low blockage based on superposition of self-similar far-wake velocity deficit profiles, Renewable Energy 92 (2016) 366–375.

O. A. Lo Brutto, J. Thiébot, S. S. Guillou, H. Gualous, A semi-analytic method to optimize tidal farm layouts – Application to the Alderney Race (Raz Blanchard), France, Applied Energy 183 (2016) 1168–1180.

E. González-Gorbeña, R. Y. Qassim, P. C. Rosman, Optimisation of hydrokinetic turbine array layouts via surrogate modelling, Renewable Energy 93 (2016) 45–57.

F. Rathgeber, D. A. Ham, L. Mitchell, M. Lange, F. Luporini, A. T. T. Mcrae, G.-T. Bercea, G. R. Markall, P. H. J. Kelly, Firedrake: Automating the finite element method by composing abstractions, ACM Trans. Math. Softw. 43 (2016) 24:1–24:27.

T. Kärnä, S. C. Kramer, L. Mitchell, D. A. Ham, M. D. Piggott, A. M. Baptista, Thetis coastal ocean model: discontinuous galerkin discretization for the three-dimensional hydrostatic equations, Geoscientific Model Development Discussions 2018 (2018) 1–36.

A. Angeloudis, S. C. Kramer, A. Avdis, M. D. Piggott, Optimising tidal range power plant operation, Applied Energy 212 (2018) 680 – 690.

F. Harcourt, A. Angeloudis, M. D. Piggott, Utilising the flexible generation potential of tidal range power plants to optimise economic value, Applied Energy 237 (2019) 873 – 884.

L. Mackie, P. S. Evans, M. J. Harrold, T. O'Doherty, M. D. Piggott, A. Angeloudis, Modelling an energetic tidal strait: investigating implications of common numerical configuration choices, Applied Ocean Research 108 (2021) 102494.

T. Karna, B. de Brye, O. Gourgue, J. Lambrechts, R. Comblen, V. Legat, E. Deleersnijder, A fully implicit wetting–drying method for DG-FEM shallow water models, with an application to the Scheldt Estuary, Computer Methods in Applied Mechanics and Engineering 200 (2011) 509–524.

S. Balay, S. Abhyankar, M. F. Adams, J. Brown, P. Brune, K. Buschelman, L. Dalcin, V. Eijkhout, W. D. Gropp, D. Kaushik, M. G. Knepley, L. C. McInnes, K. Rupp, B. F. Smith, S. Zampini, H. Zhang, H. Zhang, PETSc Users Manual, Technical Report ANL-95/11 - Revision 3.7, Argonne National Laboratory, 2016. URL: `http://www.mcs.anl.gov/petsc`.

S. C. Kramer, M. D. Piggott, A correction to the enhanced bottom drag parameterisation of tidal turbines, Renewable Energy 92 (2016) 385–396.

R. Martin-Short, J. Hill, S. C. Kramer, A. Avdis, P. A. Allison, M. D. Piggott, Tidal resource extraction in the Pentland Firth, UK: Potential impacts on flow regime and sediment transport in the Inner Sound of Stroma, Renewable Energy 76 (2015) 596–607.

T. Schwedes, D. A. Ham, S. W. Funke, M. D. Piggott, An application: Optimising the layout of tidal turbine arrays, in: Mesh Dependence in PDE-Constrained Optimisation: An Application in Tidal Turbine Array Layouts, 1 ed., Springer, 2017, pp. 79–107.

NREL, FLORIS. Version 2.2.0, 2020. URL: `https://github.com/NREL/floris`.

M. Bastankhah, F. Porté-Agel, A new analytical model for wind-turbine wakes, Renewable Energy 70 (2014) 116–123.

A. Niayifar, F. Porté-Agel, Analytical modeling of wind farms: A new approach for power prediction, Energies 9 (2016) 1–13.

N. O. Jensen, A Note on Wind Generator Interaction, Technical Report, Risø National Laboratory, Roskilde, 1983.

N. Dufresne, M. Wosnik, Velocity deficit and swirl in the turbulent wake of a wind turbine, Marine Technology Society Journal 47 (2013) 193–205.

L. P. Chamorro, F. Porté-Agel, A wind-tunnel investigation of wind-turbine wakes: Boundary-Layer turbulence effects, Boundary-Layer Meteorology 132 (2009) 129–149.

E. Machefaux, G. C. Larsen, J. P. Leon, Engineering models for merging wakes in wind farm optimization applications, Journal of Physics: Conference Series 625 (2015).

P. A. Fleming, A. Ning, P. M. Gebraad, K. Dykes, Wind plant system engineering through optimization of layout and yaw control, Wind Energy 19 (2016) 329–344.

P. M. O. Gebraad, F. W. Teeuwiise, J. W. van Wingerden, P. A. Fleming, S. D. Ruben, J. R. Marden, L. Y. Pao, Wind plant power optimization through yaw control using a parametric model for wake effects—a CFD simulation study, Wind Energy 19 (2014) 95–114.

D. Kraft, A Software Package for Sequential Quadratic Programming, Technical Report 28, Institut für Dynamik der Flugsysteme, 1988.

SIMEC Atlantis Energy, Tidal Turbines, 2020. URL: `https://simecatlantis.com/services/turbines/`, [Accessed 18 Nov. 2020].

SIMEC Atlantis Energy, AR1500 Tidal Turbine Brochure, 2016. URL: `https://www.atlantisresourcesltd.com/wp/wp-content/uploads/2016/08/AR1500-Brochure-Final-1.pdf`, [Accessed 16 Nov. 2020].

T. Stallard, T. Feng, P. K. Stansby, Experimental study of the mean wake of a tidal stream rotor in a shallow turbulent flow, Journal of Fluids and Structures 54 (2015) 235–246.

A. S. Bahaj, A. F. Molland, J. R. Chaplin, W. M. J. Batten, Power and thrust measurements of marine current turbines under various hydrodynamic flow conditions in a cavitation tunnel and a towing tank, Renewable Energy 32 (2007) 407–426.

R. Wituła, D. Słota, Cardano's formula, square roots, chebyshev polynomials and radicals, Journal of Mathematical Analysis and Applications 363 (2010) 639–647.

A. Crespo, J. Hernández, Turbulence characteristics in wind-turbine wakes, Journal of Wind Engineering and Industrial Aerodynamics 61 (1996) 71–85.

D. Coles, C. Greenwood, A. Vogler, T. Walsh, D. Taaffe, Assessment of the turbulent flow upstream of the Meygen Phase 1A tidal stream turbines, 2018.

J. Hardwick, I. Ashton, L. Johanning, Field characterisation of currents and near surface eddies in the Pentland Firth, in: Proceedings of the 4th Oxford Tidal Energy Workshop, March, 2015, pp. 34–35.

P. Virtanen, R. Gommers, T. E. Oliphant, M. Haberland, T. Reddy, D. Cournapeau, E. Burovski, P. Peterson, W. Weckesser, J. Bright, S. J. van der Walt, M. Brett, J. Wilson, K. J. Millman, N. Mayorov, A. R. J. Nelson, E. Jones, R. Kern, E. Larson, C. J. Carey, İ. Polat, Y. Feng, E. W. Moore, J. VanderPlas, D. Laxalde, J. Perktold, R. Cimrman, I. Henriksen, E. A. Quintero, C. R. Harris, A. M. Archibald, A. H. Ribeiro, F. Pedregosa, P. van Mulbregt, SciPy 1.0 Contributors, SciPy 1.0: Fundamental Algorithms for Scientific Computing in Python, Nature Methods 17 (2020) 261–272.

J. Sandoval, K. Soto-Rivas, C. Gotelli, C. Escauriaza, Modeling the wake dynamics of a marine hydrokinetic turbine using different actuator representations, Ocean Engineering 222 (2021).

T. Stallard, R. Collings, T. Feng, J. Whelan, Interactions between tidal turbine wakes: Experimental study of a group of three-bladed rotors, Philosophical Transactions of the Royal Society A: Mathematical, Physical and Engineering Sciences 371 (2013).

A. Avdis, A. S. Candy, J. Hill, S. C. Kramer, M. D. Piggott, Efficient unstructured mesh generation for marine renewable energy applications, Renewable Energy 116 (2018) 842–856.

C. V. Vouriot, A. Angeloudis, S. C. Kramer, M. D. Piggott, Fate of large-scale vortices in idealized tidal lagoons, Environmental Fluid Mechanics 19 (2019) 329–348.

S. Draper, T. A. Adcock, A. G. Borthwick, G. T. Houlsby, Estimate of the tidal stream power resource of the Pentland Firth, Renewable Energy 63 (2014) 650–657.

Edina Digimap Service, Hydrospatial one, gridded bathymetry, `http://digimap.edina.ac.uk/marine/`, 2020. , SeaZone Solutions Ltd, Online; accessed 2020.

T. A. Adcock, S. Draper, G. T. Houlsby, A. G. Borthwick, S. Serhadlioğlu, The available power from tidal stream turbines in the pentland firth, Proceedings of the Royal Society A: Mathematical, Physical and Engineering Sciences 469 (2013).

R. O'Hara Murray, A. Gallego, A modelling study of the tidal stream resource of the Pentland Firth, Scotland, Renewable Energy 102 (2017) 326–340.

R. Martin-Short, J. Hill, S. Kramer, A. Avdis, P. Allison, M. Piggott, Tidal resource extraction in the pentland firth, uk: Potential impacts on flow regime and sediment transport in the inner sound of stroma, Renewable Energy 76 (2015) 596 – 607.

G. D. Egbert, S. Y. Erofeeva, Efficient inverse modeling of barotropic ocean tides, Journal of Atmospheric and Oceanic Technology 19 (2002) 183–204.

D. Coles, L. Blunden, A. Bahaj, Assessment of the energy extraction potential at tidal sites around the channel islands, Energy 124 (2017) 171–186.

M. De Dominicis, J. Wolf, R. O'Hara Murray, Comparative effects of climate change and tidal stream energy extraction in a shelf sea, Journal of Geophysical Research: Oceans 123 (2018) 5041–5067.

E. Branlard, A. R. Meyer Forsting, Assessing the blockage effect of wind turbines and wind farms using an analytical vortex model, Wind Energy 23 (2020) 2068–2086.

P. Ouro, L. Ramírez, M. Harrold, Analysis of array spacing on tidal stream turbine farm performance using large-eddy simulation, Journal of Fluids and Structures 91 (2019) 102732.

T. Nishino, R. H. Willden, Two-scale dynamics of flow past a partial cross-stream array of tidal turbines, Journal of Fluid Mechanics 730 (2013) 220–244.

P. K. Stansby, A mixing-length model for shallow turbulent wakes, Journal of Fluid Mechanics 495 (2003) 369–384.

L. Zong, H. Nepf, Vortex development behind a finite porous obstruction in a channel, Journal of Fluid Mechanics 691 (2012) 368–391.

M. A. Abolghasemi, M. D. Piggott, J. Spinneken, A. Viré, C. J. Cotter, S. Crammond, Simulating tidal turbines with multi-scale mesh optimisation techniques, Journal of Fluids and Structures 66 (2016) 69 – 90.

G. Deskos, M. A. Abolghasemi, M. D. Piggott, Wake predictions from two turbine models using mesh-optimisation techniques, in: A. Lewis (Ed.), Proceedings of the Twelfth European Wave and Tidal Energy Conference, EWTEC, University College Cork, Ireland, 2017. ISSN: 2309-1983.

M. J. Churchfield, Y. Li, P. J. Moriarty, A large-eddy simulation study of wake propagation and power production in an array of tidal-current turbines, Philosophical Transactions of the Royal Society of London A: Mathematical, Physical and Engineering Sciences 371 (2013).

M. Thiébaut, J. F. Filipot, C. Maisondieu, G. Damblans, C. Jochum, L. F. Kilcher, S. Guillou, Characterization of the vertical evolution of the three-dimensional turbulence for fatigue design of tidal turbines: 3D turbulence for fatigue design of TEC, Philosophical Transactions of the Royal Society A: Mathematical, Physical and Engineering Sciences 378 (2020).

D. S. Coles, L. S. Blunden, A. S. Bahaj, The energy yield potential of a large tidal stream turbine array in the alderney race, Philosophical Transactions of the Royal Society A: Mathematical, Physical and Engineering Sciences 378 (2020) 20190502.

G. Deskos, S. Laizet, R. Palacios, Winc3d: A novel framework for turbulence-resolving simulations of wind farm wake interactions, Wind Energy 23 (2020) 779–794.